ADVANCED MATERIALS
www.advmat.de

Ultraflexible Vertical Corbino Organic Electrochemical Transistors for Epidermal Signal Monitoring

Inho Lee, Ji Hwan Kim, Youngseok Kim, Dongjoon Shin, Hyeongbeom Lee, Jonghyun Won, Keehoon Kang, Jun-Gyu Choi, Myung-Han Yoon, and Sungjun Park**

Skin-conformal organic electrochemical transistors (OECTs) have attracted significant attention for real-time physiological signal monitoring and are vital for health diagnostics and treatments. However, mechanical harmonization amid the inherent dynamic nature of the skin surface and the acquisition of intrinsic physiological signals are significant challenges that hinder the integration of the ultimate skin interface. Thus, this study proposes a novel 4-terminal (4-T) vertical Corbino OECT, exhibiting high transconductance (>400 mS) and offering remarkable resilience and operational stability at an extremely low voltage of 10 mV (1.9% of minimal current change after 10^4 biasing cycles and endurance up to 10^3 cycles of repetitive deformation with a 5 µm bending radius). Consequently, ultralow-power, motion-resistant epidermal electrocardiogram, electromyogram, and electrooculogram sensors are developed with an exceptional signal-to-noise ratio of 40.1 dB. The results of this study present a significant stride in non-invasive, skin-interfaced health-monitoring technologies and herald a new era in integrative health technologies.

1. Introduction

Ultraflexible organic electrochemical transistors (OECTs) are considered potential pivotal elements that facilitate physiological signal monitoring owing to their distinct attributes, including high sensitivity,[1–3] mechanical flexibility,[4–7] and biocompatibility.[8–11] Their unique ability to interlink ionic and electronic charges allows their effective operation at the ion-rich interfaces of skin and tissue, wherein, subtle electrochemical physiological signals are converted into electrical outputs with instrument compatibility.[12–15] For optimal bio-interfacing, several key factors must be addressed. 1) Enhanced amplification at minimal operating voltages, achievable by eliminating parasitic resistances to minimize the energy loss and foster an effective conduction path, 2) A rapid response time paired with an expansive cutoff frequency range where an optimized spatial design in the volumetric occupancy of the active layer can enhance ion transport and redox reaction efficacy, 3) robust mechanical resilience, given the dynamic nature of human skin, that remains unaffected by motion-induced distortions, necessitating isotropic channel designs to withstand multidirectional stresses and finally, 4) seamless adhesion to intricate skin topographies facilitated with an ultrathin design of minimal flexural rigidity, enabling a reliable and seamless human-machine interface to adhere to various skin textures without bending or fractures. Thus, to achieve optimal bio-interfacing with electronic devices, it is essential to strike a balance between electrical performance and geometrical constraints within a limited space while ensuring consistent functionality even under mechanical stress.

State-of-the-art OECTs have achieved profound advancements, with high transconductance (g_m) values of 384 mS and cutoff frequencies (f_c) of 1.2 kHz.[16] Such advances are attributed to the innovative use of redox-active semiconducting polymers blended with a redox-inert and photocurable polymer component in a vertical architecture, which facilitates long-term and rapid switching operations, demonstrating high-performance complementary circuits on a rigid substrate. Considering the flexibility benchmark, several flexible OECTs have been manifested on few-µm-thick polymeric substrates with transconductance values of a few tens of millisiemens (g_m <70 mS)[17] and cutoff frequencies lower than 560 Hz.[4] These devices also show potential for accurate sensing of physiological signals at skin and tissue surfaces.[8,18–22]

Despite these advancements, efforts to improve device performance often face limitations due to a trade-off related to channel

I. Lee, D. Shin, H. Lee, J. Won, S. Park
Department of Intelligence Semiconductor
Ajou University
Suwon, Gyeonggi-do 16499, Republic of Korea
E-mail: sj0223park@ajou.ac.kr
J. H. Kim, K. Kang
Department of Materials Science and Engineering
Seoul National University
Seoul 08826, Republic of Korea
Y. Kim, M.-H. Yoon
School of Materials Science and Engineering
Gwangju Institute of Science and Technology (GIST)
Gwangju 61005, Republic of Korea
E-mail: mhyoon@gist.ac.kr
J.-G. Choi, S. Park
Department of Electrical and Computer Engineering
Ajou University
Suwon 16499, Republic of Korea

The ORCID identification number(s) for the author(s) of this article can be found under https://doi.org/10.1002/adma.202410444

DOI: 10.1002/adma.202410444

geometry and applied bias, regardless of intrinsic material characteristics. One strategy to increase the g_m value involves enlarging the geometric factor, Wd/L, of the channel according to the well-known dependence of g_m, $g_m = (Wd/L) \times (\mu C^*) \times (V_G - V_{Th})$, where μ represents the mobility, and C^* is the volumetric capacitance, and W, d, and L are the channel's geometric dimensions. V_G denotes the gate voltage (the electrical potential difference between the gate and source terminals), and V_{Th} is the threshold voltage. This strategy is often realized by fabricating vertical OECT architecture. However, as the channel resistance (R_{Ch}) decreases following $R_{Ch} = \rho_{Ch} \times (L/Wd)$ with an increasing Wd/L, the relative IR drop at the parasitic resistance ($R_{Contact}$ and R_{Line}) correspondingly increases. Consequently, even if g_m improves with Wd/L, the degree is limited by the increasing relative IR drop across the parasitic resistance components. Furthermore, the device response time generally slows down as Wd/L increases[23,24] (inversely proportional to $d(LW)^{0.5}$). As Maciej Gryszel and his colleagues clearly demonstrated, vertical OECTs require a smaller volume of channel materials, resulting in a switching time of 16–20 times faster than that of planar OECTs.[25] In addition, conventional rectangular and large Wd/L channel geometry introduces anisotropic mechanical strain during dynamic skin motion, impeding efficient charge transport through the channel.[26] Therefore, addressing the trade-off between channel geometry and g_m, response time, and mechanical robustness simultaneously presents a considerable challenge.

This study proposed a motion-robust and skin-conformal ultraflexible 4-terminal vertical Corbino organic electrochemical transistor (4-T vcOECT). The introduction of the 4-T architecture eliminated redundant parasitic resistances to optimize the g_m value, thus providing an independent platform for extracting intrinsic electrical parameters. Furthermore, a vertical Corbino architecture resulted in impressive g_m and f_c values by maximizing the geometrical parameters (Wd/L), and exceptional mechanical durability attributed to the isotropic stress distribution even under significant strain. The resultant device yielded record-high g_m values exceeding 400 mS and increased cutoff frequencies (f_c) up to 2 kHz. A negligible change in total current was observed after 10^4 biasing cycles, and repetitive deformations up to 10^3 cycles with a tight bending radius of 5 µm. Owing to its small radial channel structure with extremely high g_m, 4-T vcOECTs ensure uniform detection of locally fluctuated ion concentrations on the small channel region, which enables reliable and accurate detection of physiological signals, including electrocardiogram (ECG), electromyogram (EMG), and electrooculogram (EOG) while operating at only 10 mV with an outstanding signal-to-noise ratio of 40.1 dB. This advancement will be instrumental in developing high-performance, ultralow-power, and motion-tolerant epidermal sensors.

2. Design of Ultraflexible 4-Terminal Vertical Corbino OECT (4-T vcOECT)

Figure 1a,b presents schematic representation and corresponding equivalent circuit diagram of the 4-terminal vertical Corbino OECT (4-T vcOECT) devices. The design drew inspiration from the four-point probe method, aiming to minimize parasitic resistance during measurements. This strategy enhances the accuracy of device characterization by reducing the influence of extraneous resistances. Two of the four terminals are dedicated to applying current (I_{Source} and I_{Drain}), facilitating the entry and exit of current through these terminals. The other two terminals are allocated for voltage measurement ($V_{Sense,1}$ and $V_{Sense,2}$), ensuring no current flows through them owing to the high electrical impedance of the voltmeter. The operation principle of the 4-T vcOECT slightly deviates from the conventional approach. In this method, the voltage between the sensing terminals ($V_{Sense,1}$ and $V_{Sense,2}$) is constant, unaffected by the current applied between the I_{Source} and I_{Drain} terminals, assuming negligible line resistance. Consequently, the I_D value displayed in the transfer curve accurately represents the current between the I_{Source} and I_{Drain} terminals. This ensures that the voltage measured between $V_{Sense,1}$ and $V_{Sense,2}$ accurately reflects the set V_D value (e.g., −0.6 V, as shown in Figure 1f) without any loss due to line resistance. Instead of applying the voltage, a current is applied between I_{Source} and I_{Drain} terminals to ensure that the voltage measured between the two sensing terminals ($V_{Sense,1}$ and $V_{Sense,2}$) reaches the set V_D value. During operation, the IR drop at $R_{Line,V1,}$ and $R_{Line,V2}$ is nullified since no current flows through the $V_{Sence,1}$ and $V_{Sense,2}$ lines, attributed to the high impedance of the voltmeter. Consequently, the voltage measured between $V_{Sense,1}$ and $V_{Sense,2}$ is confined to the series resistance of $R_{Contact,S}$, R_{Ch}, and $R_{Contact,D}$, excluding $R_{Line,S}$ and $R_{Line,D}$. As the current source delivers current until the voltage value matches the V_D, it effectively evaluates V_D across the series resistance of $R_{Contact,S}$, R_{Ch}, and $R_{Contact,D}$, disregarding line resistances. All devices can be measured using a conventional source−measure unit in 4-wire mode without the need for any additional measurement setup or equipment (Figure S1, Supporting Information).

The vertical Corbino structure is defined by a patterned via hole that exists between the top and bottom metal electrodes (the upper and lower layers serve as the drain and source electrode, respectively) through the parylene-C (PaC) layer (Figure 1c). This design allowed the channel to be distinctly delineated on the sidewalls of the circular holes, thereby optimizing the device footprint. Consequently, the channel length and width could be precisely controlled by adjusting the thickness of the PaC layer (T_{PaC}) and the perimeter ($2\pi r$) of the via holes, respectively.[25–27] This innovative design facilitates operation in both accumulation and depletion modes with efficient redox reaction of the whole active channel exposed to electrolytes. Incorporating vertical and Corbino structured devices on a 1-µm-thick ultraflexible PaC substrate enables isotropic strain distribution, fully leveraging the device's thinness for highly sensitive physiological monitoring. These features significantly improve the sensitivity and adaptability, particularly when interfaced with skin and tissue surfaces. Figure 1d shows a cross-sectional transmission electron microscopy (TEM) image illustrating the vertical geometry of the 4-T vcOECT. The channel length of the OECT, represented by T_{PaC}, was quantified to be ≈500 nm, as determined by both the analysis of the TEM image and the surface profiler (Figure S2, Supporting Information). Figure 1e shows a photograph of an ultraflexible 4-T vcOECT on a SU-8/PaC substrate after being peeled off from the supporting glass substrate. The 1.2-µm-thick ultrathin SU-8/PaC substrate enabled the transfer and attachment of the 4-T vcOECT device onto complex surface, including human skin. The floral pattern does not serve a specific functional role related to the structure of the 4-terminal

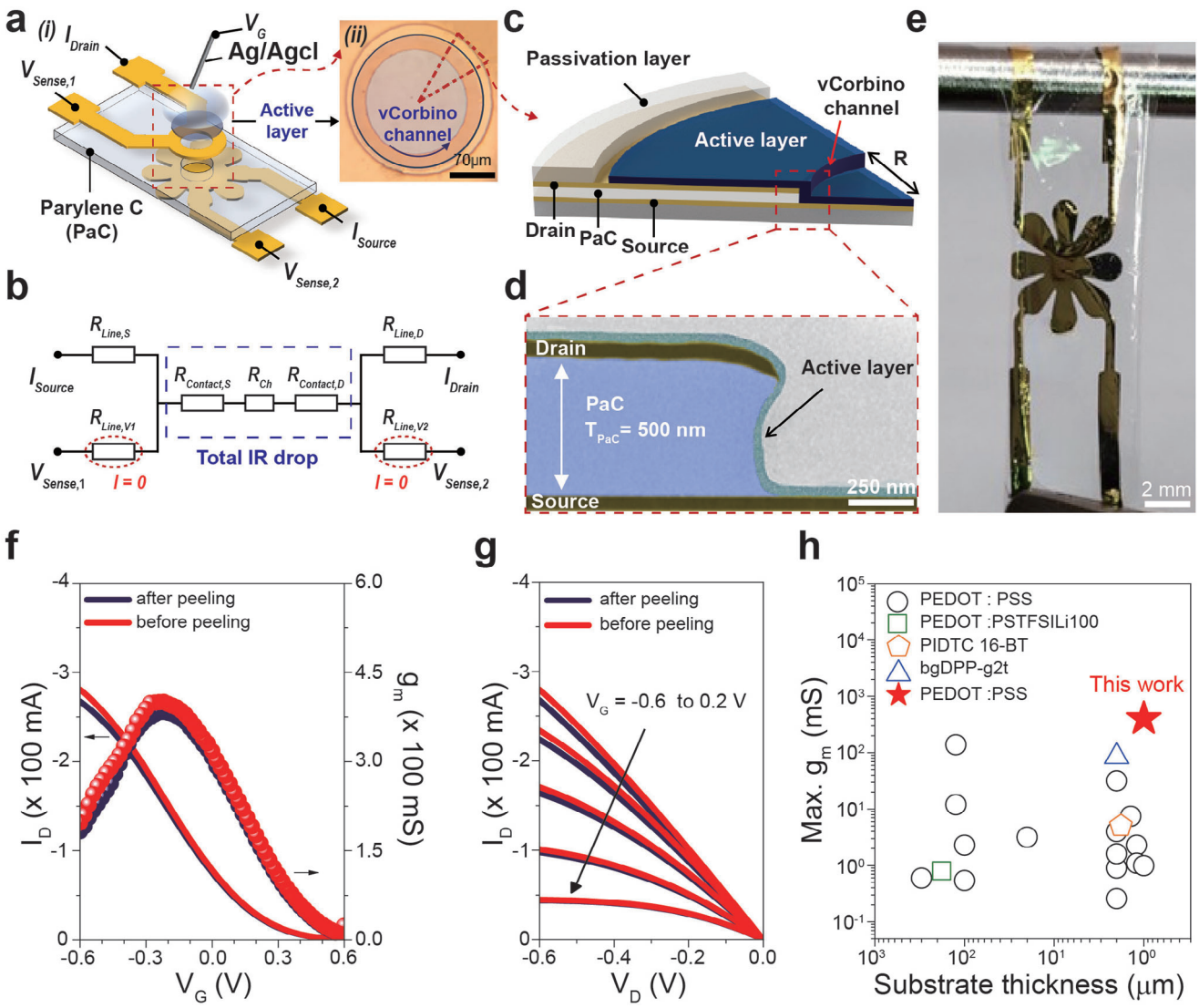

Figure 1. Design of Ultraflexible vcOECT and electrical performance. a) i) Schematic of the 4-T vcOECT device configuration. ii) Enlarged view of the channel region featuring the vertical Corbino structure. b) Equivalent circuit diagram of the 4-T vcOECT device. c) Schematic of channel region of vcOECT device. d) High-resolution cross-sectional transmission electron microscopy (TEM) image of channel region of the vcOECT. e) Photograph of the ultraflexible 4-T vcOECT wrapped over a spatula rod. f) Transfer curve and g_m values before(red) and after(blue) peeling off. g) Output curve before (red) and after (blue) peeling off (channel $R = 70$ μm; $L = 500$ nm; $d = 80$ nm). h), Comparison of maximum transconductance values among reported flexible OECTs, as a function of the substrate thickness.

vertical Corbino, but it highlights the importance of aesthetics, which is an essential aspect of bioelectronics in skin engineering. The fabrication process is detailed in the Supporting Information (Figures S3 and S4, Supporting Information). When reducing the channel length to 500 nm with a vertical structure, the transconductance value dramatically increased by more than eight times compared with a planar type of relatively long channel length OECT (Figure S5, Supporting Information) at the same channel width. Figure 1f,g shows the transfer (sweeping V_G from −0.6 to 0.6 V with $V_D = -0.6$ V) and output (sweeping the drain-source bias, V_D, from 0 to −0.6 V, and stepping the gate-source bias, V_G, from −0.6 to 0.2 V) characteristic curves of the ultraflexible 4-T vcOECTs with a channel length of 500 nm and Corbino radius of 70 μm before and after delamination from the supporting glass substrate. As evident, our ultraflexible 4-T vcOECT exhibited unprecedented g_m values of 392 ± 8 mS and max 400 mS compared to other state-of-the-art rigid and flexible *p*-type OECTs, achieving an accurate measurement without the influence of parasitic resistance (Figure 1h; Figures S5–S7 and Tables S1, S2, and S5, Supporting Information).

3. Electrical Characterization of 4-T vcOECT

For the electrical characterization and analysis of the 4-T vcOECTs, as shown in **Figure 2**a, it is noted that the total resistance R_{Total} can be contributed from the channel (R_{Ch}), metal line (R_L), and the interfacial resistance (R_C) between the active and metal layers, all in series. Consequently, the R_{Total} values of

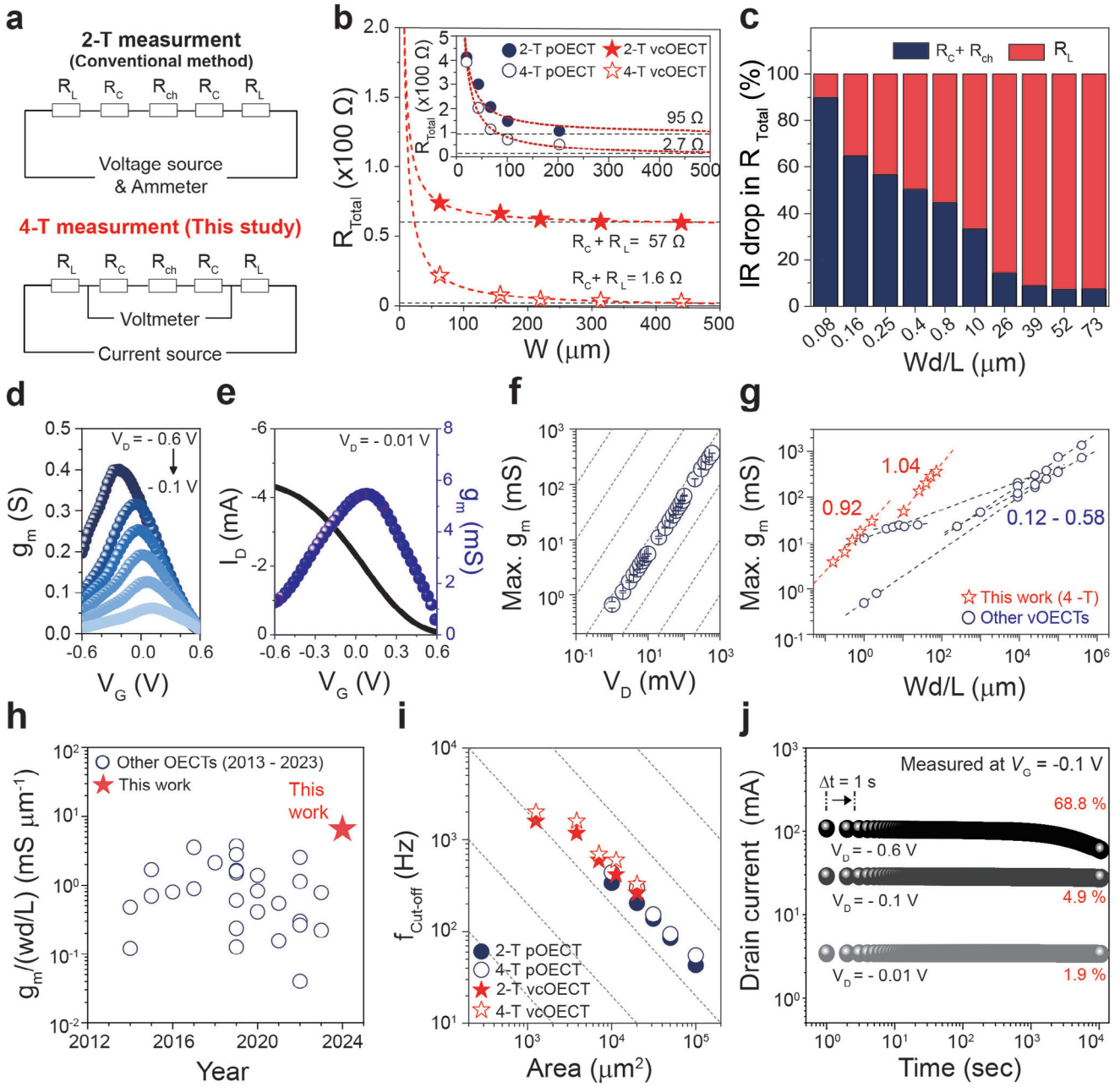

Figure 2. Electrical characterization of 4-T vcOECT. a) Circuit diagram comparison of 2-T (top) and 4-T (bottom) measurement configuration. b) Comparison of total resistance between 2-T and 4-T OECT according to channel width. c) Relative *IR* drop at channel and metal line as a function of *Wd*/*L*. d) g_m values according to drain voltage −0.6 to −0.1 V. e) Transfer curve and transconductance values at drain voltage −0.01 V. f) g_m values increase linearly with drain voltage (R = 70 μm, L = 500 nm, and d = 80 nm). g) g_m values as a function of *Wd*/*L*, obtained from vcOECT (red star) and pOECT (black square). Filled and empty symbols indicate those measured by 2-T and 4-T method, respectively. h) g_m value normalized by *Wd*/*L* plot reported from 2013–2023. i) Frequency response of pOECTs and vcOECTs. j) Operational stability of 4-T vcOECT at different V_D = −0.6, −0.1, and −0.01 V. V_G is switched between 0.1 and −0.1 V and extracted I_D at V_G = −0.1 V were displayed.

2-T and 4-T configurations are characterized as $R_{Ch} + R_L + R_C$ and $R_{Ch} + R_C$, respectively. To assess the impact of parasitic resistance on high g_m OECT devices, we first prepared various planar and vertical devices with different geometrical factors (*Wd*/*L*), ranging from 0.08 to 73 μm. Subsequently, R_{Total} was extracted from the transfer characteristics in the saturation regime (at $V_D > V_G - V_T$), as detailed in Note S1 (Supporting Information).

The extracted all R_{Total} values for 2-T (open symbol) and 4-T (open symbol) configurations are plotted as a function of W (Note S2, Supporting Information) for vertical (indicated by red stars) and planar OECTs (pOECTs, dark navy circles) in Figure 2b. The 2-T pOECTs exhibited parasitic resistance ($R_C + R_L$) of ≈ 95 Ω, while 4-T pOECTs showed a significantly lower resistance (R_C) of ≈2.7 Ω, underscoring the efficacy of the 4-T measurement

configuration in reducing R_L. Due to differences in line patterns between pOECT and vcOECT (Figure S8 and Note S3, Supporting Information), the reduction in line resistance is less pronounced in vcOECTs (57 Ω for 2-T vcOECT and 1.6 Ω for 4-T vcOECT, respectively). However, as Wd/L value increases, the influence of parasitic resistance becomes more dominant. This effect is visualized in Figure 2c, which plots the ratio of potential drop at the active material (R_{Ch} + R_C) and metal electrode (R_L) as a function of Wd/L (Note S1 and Figure S9, Supporting Information). These results indicate that in a 2-T configuration, the applied potential from the voltage source is not fully exerted in the active channel. In contrast, 4-T configuration compensates for the potential drop along the metal line using a potentiostat, ensuring that the designated potential level is effectively applied to the channel region, free from parasitic line resistance.

The electrical properties of the 4-T vcOECT devices were characterized. As shown in Figure 2d, the transfer characteristics with V_D varying from −0.6 to −0.1 V were analyzed. The peak g_m value at V_D = −0.6 V (dark navy) reached over 400 mS, representing the highest metric among reported PEDOT: PSS-based OECT devices, to our knowledge.[28–31] With V_D decreased to −0.1 V and then further to −0.01 V, the corresponding peak g_m values exhibited 62.3 mS (Figure 2e) and 5.8 mS (Figure 2f; Figure S10, Supporting Information). Remarkably, the g_m at the low operation voltage of V_D = −0.01 V was still higher than that of conventional planar OECT devices operating at V_D above −0.6 V[14,20,32–34] (Tables S1 and S2, Supporting Information). This indicates both superior performance and low power consumption in device operation. Moreover, a clear monotonic trend of the g_m value with increasing V_D proves the minute controllability of g_m, allowing easy calibration, tunable sensitivity, and high resolution for signal acquisition. Additionally, the variation in peak g_m relative to the dimensional factor (Wd/L, at V_G = −0.6 V, Figure 2g; Figures S11–S13, Supporting Information) showed a consistent increase with a slope of 1, spanning a Wd/L range from 10 to 70 µm. This range corresponds to the radius of the Corbino structure varying from 10, 25, 37.5, 50, to 70 µm, indicating that even when the width is minimized down to 62.8 µm (R = 10 µm), a high g_m of ≈49 mS was achieved. This result confirms that the vcOECT operates under conditions where parasitic resistance is significantly minimized. Mixed conduction figure of merit (μC^*) was extracted, yielding values of 210, 102, 71, and 4.6 F cm^{-1} V^{-1} s^{-1} for the 4-T pOECT, 2-T pOECT, 4-T vcOECT, and 2-T vcOECT, respectively. As discussed in Figure 2c, this decrease in μC^* with increasing Wd/L value is also attributed to the increasing IR drop due to parasitic resistance, diminishing effective voltage applied to the channel. The logarithmic plot of g_m versus Wd/L of our device was compared with those of other representative vertical OECTs as shown in Figure 2g and Figure S13 (Supporting Information). Our vcOECTs, measured by the 4-T configuration, exhibited a slope of ≈1, while the values for other vOECTs range from 0.12 to 0.58. A significantly lower value of 0.29 for 2-T configuration of our vcOECTs reflects the significant impact of IR drop at parasitic resistance as Wd/L increases (Figure S13, Supporting Information). This pattern is consistent with recent research on vertical OECT structures for complementary circuits, which reported slopes of 0.31 to 0.58 for *p*-type and *n*-type materials,[16,31,35] highlighting the impact of parasitic resistance. On the contrary, devices measured in a 4-T configuration exhibited the highest slope values. This suggests that with further increases in Wd/L, the g_m value of OECT devices is anticipated to surpass previously reported values. In addition, the 4-T OECT maintains relatively high μC^* values, despite the challenges associated with the high Wd/L values. These findings confirm that the 4-T configuration effectively addresses the problem of parasitic resistance, thereby enabling more accurate extraction of intrinsic charge transport properties, even in devices with high Wd/L values.

Additionally, we normalized g_m values by Wd/L, comparing them to reported works to date (Figure 2h). This comparison covered vertical and planar OECT devices with Wd/L values over 10 (Table S3, Supporting Information) since devices with lower Wd/L values are less affected by parasitic resistance. The normalized g_m value in our work, obtained via the 4-T measurement configuration, demonstrated the highest value. This underscores the importance of reducing parasitic resistance in OECTs with high Wd/L values (including vOECTs) for accurately assessing the intrinsic g_m value of OECTs.

Ideally, the f_c values are inversely proportional to the volume of the channel.[36] Due to the minimized spatial occupation of an active layer in the confined structure of vcOECTs,[27] the minimized channel volume leads to an enhanced cutoff frequency (f_c) reaching up to 2 kHz (Figure 2i; Figures S14–S16 and Table S4, Supporting Information). The 6.1-fold increase in f_c, despite a 2.6-fold decrease in $d(WL)^{0.5}$, is attributed to the increased ion resistivity of the channel, which results from the crystallized structure of PEDOT:PSS, induced by the incorporation of ethylene glycol and DBSA during film preparation. Structural factors such as degree of crystallinity, crystallite size, and molecular orientation influence the ionic mobility of OMIECs,[37–39] which in turn affects the transit time of OECTs. Additionally, vcOECTs utilize an edge-on molecular orientation, which is optimal for facilitating ion transport in the out-of-plane direction and charge carrier transport in the in-plane direction. This arrangement significantly impacts both efficient charge carrier transport and the rapid transient response of the device.[40,41] The 4-T (open symbol) configuration exhibits a higher transient response (as high as 110%) compared to 2-T configuration due to the effective nullification of line resistance, indicating potential of accurate and stable measurements for various physiological signals. The rise and fall times of 4-T vcOECTs, measured across various channel widths (Figure S17, Supporting Information), exhibited rise times of 343 µs and fall times of 98 µs when the width is minimized down to 62.8 µm (R = 10 µm). This fast response in vcOECTs is attributable to the low $d(LW)^{0.5}$ value, which facilitates ion drift into the channel due to the short ion diffusion length,[41] comparable to the thickness of the PEDOT:PSS channel (≈80 nm). To assess the long-term operational stability of the device, the I_D was monitored under different V_D conditions by periodically applying voltages of +0.1 and −0.1 V to the gate electrode under repetitive gate bias switching (V_D = −0.6, −0.1, and −0.01 V, Δt = 0.5 s) as shown in Figure 2j and Figure S18 (Supporting Information). This result suggests that the device with V_D of −0.1 and −0.01 V remains stable for up to 10 000 cycles, whereas the device with a V_D of −0.6 V showed significant reductions in current values. This stems from the irreversible morphological change and chemical degradation of the polymer, caused by the significant volume expansion/shrinkage and oxygen

reduction reaction occurring in the vicinity of the drain electrode, respectively.[42,43] Additionally, the operational stability under full doping/dedoping conditions (0 to 0.6 V) was monitored at different V_D bias conditions (V_D = −0.6, −0.1, and −0.01 V) (Figure S19, Supporting Information). After 1000 cycles, the on-current values were reduced by 59%, 37%, and 31% from the initial on-current value for V_D of −0.6, −0.1, and −0.01 V, respectively. By fitting the operational stability test results with an exponential decay function (Figure S19d, Supporting Information), it is anticipated that the on-current values will diminish by 93%, 86%, and 76% from the initial on-current values for V_D of −0.6, −0.1, and −0.01 V, respectively. This suggests that minimizing the redox reaction of the active layer offers greater benefits for long-term operational stability, aligning closely with the typical operational conditions of biosignal recording.

4. Isotropic Mechanical Resilience of 4-T vcOECT

To develop a motion-robust epidermal biosignal monitoring sensor, operational stability must be ensured under mechanical deformation identical to the range of motion of the skin surface. To evaluate the mechanical stability of the ultraflexible 4-T vcOECT, we transferred the delaminated 4-T vcOECTs from the supporting glass to a pre-stretched polymeric elastomer. Consequently, the ultraflexible 4-T vcOECTs were gently laminated onto a 200% outward pre-stretched polymeric elastomer, which was pre-stretched to three times its initial size, that is, 200% tensile strain (Figure S20, Supporting Information). Upon reducing the stretching force till the initial elastomer size was reached, the tensile strain was reduced, that is, 0% tensile strain was obtained. At the same time, the vcOECTs were subjected to the compressive strain range of 0–66% by reducing the tensile strain of elastomers from 200% to 0%, respectively. Here, 0% tensile strain indicated that the pre-stretched elastomers recovered to their initial size and 66% compressive strain was applied to vcOECTs. Notably, the wrinkled surfaces of ultraflexible 4-T vcOECTs was observed as the compressive strain increased toward 66% (**Figure 3a**). The multiple wrinkles at 50% tensile strain of elastomers were observed by a 3D confocal microscope (Figure 3b). Also, the minimum radius of curvature of the multiple wrinkles was identified to be within 6 µm with a high aspect ratio proved by cross-sectional scanning electron microscopy (SEM) as shown in Figure 3c.

The electrical characteristics of ultraflexible 4-T vcOECTs were evaluated with tensile strains of 200–0% (measured with each 50% step of tensile strain). As shown in Figure 3d, the invariant electrical characteristics of the ultraflexible 4-T vcOECTs were observed with gradual mechanical deformation, attributed to the mechanical durability with uniform stress distribution at vertical channel region with circular geometry. Within a vertical structure, the current flows vertically between the bottom and the top electrodes, and mechanical deformations within the flat plane no longer impede the flow of current.[17,44] Furthermore, the circular geometry can facilitate stress dispersion regardless of direction. This enables it to effectively accommodate mechanical deformations arising from the stress applied in the diverse orientations. To confirm superb mechanical durability, we measured and compared the maximum g_m values under the variable tensile strain from 200% to 0% in the horizontal and vertical directions (Figure S20, Supporting Information) for pOECTs. The maximum g_m of the 4-T vcOECTs remained consistent with its initial values, showing no significant variation in both the horizontal and vertical directions, even after applying and releasing 66% compressive strain (Figures S21 and S22, Supporting Information). This stability suggests robust film adhesion and the absence of delamination. In contrast, the maximum g_m of the pOECTs decreased sharply, nearing zero, which we attribute to film delamination caused by the strain. For on-skin bioelectronic applications, OECTs performance should be insensitive within the range of maximum strain tolerated by human skin (≈30%).[45,46] We also tested the mechanical stability of the ultraflexible 4-T vcOECT by measuring the maximum g_m values over 1000 cycles at 100% compression strain. This was done using the same gate voltage sweep range as in Figure 3d, where the gate voltage was swept from −0.6 to +0.6 V. As shown in Figure 3e, the minimal changes in max g_m values after 1000 cycles of repeated mechanical deformation were observed at different V_D values, with reductions from 400 to 341 mS at −0.6 V and from 4.7 to 3.7 mS at −0.01 V, indicating excellent mechanical durability.

In comparison to previously reported high-performance vertical structured OECTs (Figure S23, Supporting Information), this study exhibits outstanding performance across various aspects including device structure, materials, normalized g_m, cutoff frequency, flexibility, and mechanical stability. The utilization of the vertical Corbino structure and the 4-terminal measurement configuration enabled us to surmount the channel geometry-g_m trade-off, achieving record-high normalized g_m values and rapid transient responses. Simultaneously, the device maintained its flexibility and operational stability under repetitive mechanical deformation.

5. Skin-Conformal 4-T vcOECT for ECG, EMG, and EOG Signal Monitoring

Finally, we demonstrated motion-robust detection of physiological signals (electrocardiogram (ECG), electromyography (EMG), and electrooculography (EOG)) using the ultraflexible 4-T vcOECT attached to skin surfaces (**Figure 4a**). The 4-T measurement configuration enhances the sensitivity of biosignal monitoring devices by eliminating parasitic resistance and increasing the signal-to-noise ratio (SNR). This setup minimizes electrical noise from the long line components,[8] which are typically unavoidable in connections between the device and measurement equipment. Figure 4b shows the scheme of the ultraflexible 4-T vcOECTs attached to the skin surfaces to monitor various physiological signals, such as i) on the fingertip for ECG, ii) inside the wrist for EMG, and iii) above the eyebrows for EOG. In these demonstrations, we did not implement a universal design integrating both OECTs and thin-film gate electrodes into a single device for diverse recordings, but conventional patch-type Ag/AgCl electrodes were used to measure the electrical properties of planar and vertical structured OECTs. Due to the device's ultrathin structure (less than 2 µm),[47] all devices can be tightly bound to the skin surface with a minimal gap, thus enabling a firm connection to the skin through capillary force using a droplet of phosphate-buffered saline (PBS) solution. This arrangement facilitates biosignal measurement with minimized noise. Physiological potentials, derived from potential differences between

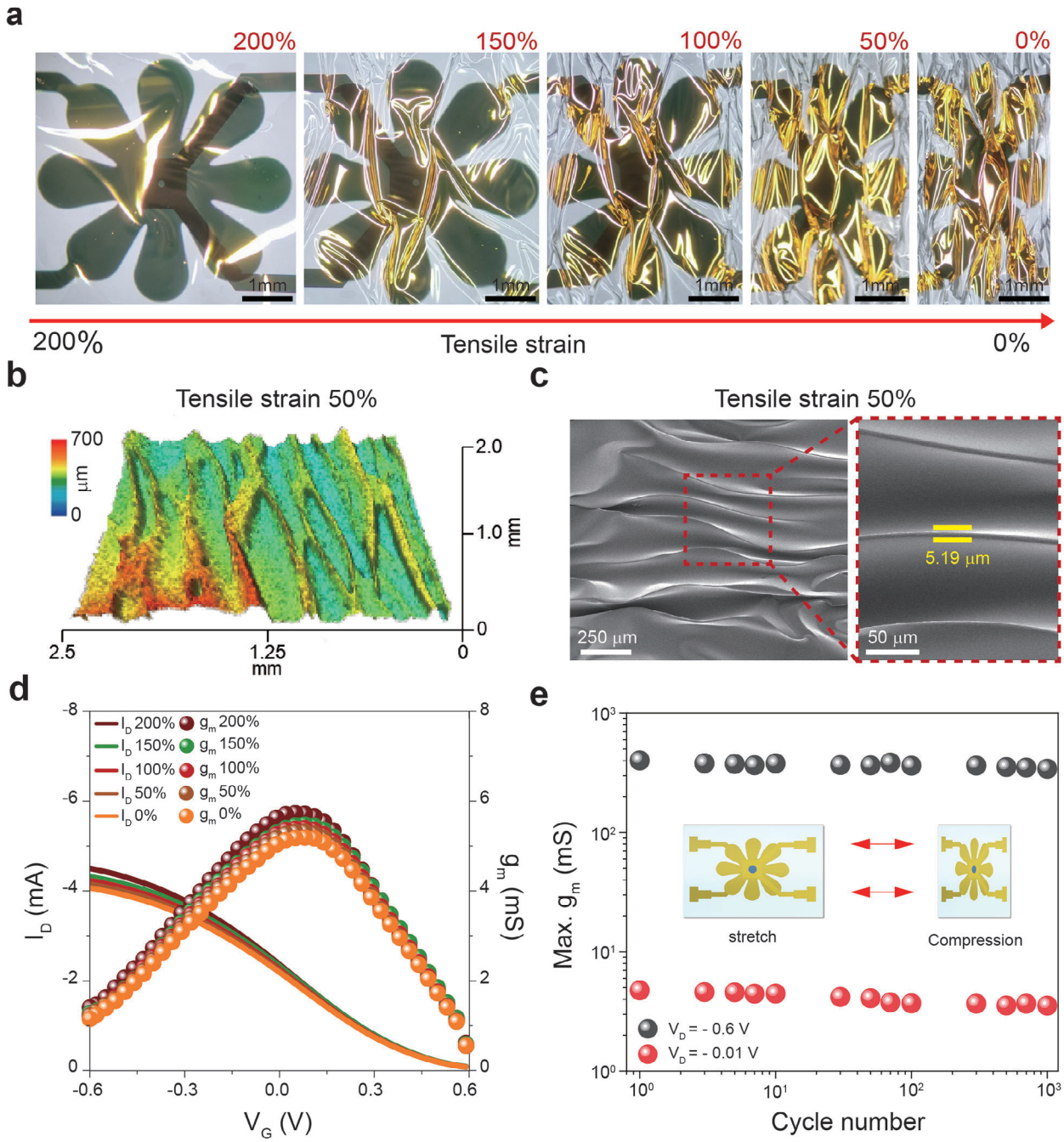

Figure 3. Long-term and operational reliability under mechanical deformation. a) Photograph with tensile strain from 200 to 0%. b) 3-D confocal microscope image of the vcOECTs undergoing 50% compressive strain. A localized sinusoidal wrinkled surface with a high aspect ratio is formed with a peak amplitude of 676 μm. c) SEM image of the vcOECT surface at 50% tensile strain (left) and magnified image showing that the bending radius is less than 6 μm (right). d) Transfer curve and transconductance characteristics under various mechanical deformations (tensile strain from 200% to 0%). e) Maximum transconductance values of ultraflexible 4-T vcOECT under repetitive cycles of compression–release (between 100% and 200%) with different V_D = −0.6, −0.01 V, respectively.

sensing and reference points, act as gate bias, triggering a redox reaction of the PEDOT:PSS channel with PBS electrolyte. This redox reaction alters the channel's conductivity, thereby transducing the physiological potential into a change in the drain current. The scheme shown in Figure 4a,b also highlights an essential aspect of on-skin bioelectronics: aesthetics. The flower-like pattern not only diminishes the sense of foreignness experienced when electronic circuits are attached to the skin but also introduces a new concept in on-skin bioelectronics, proposing the use of the device as a form of accessory.

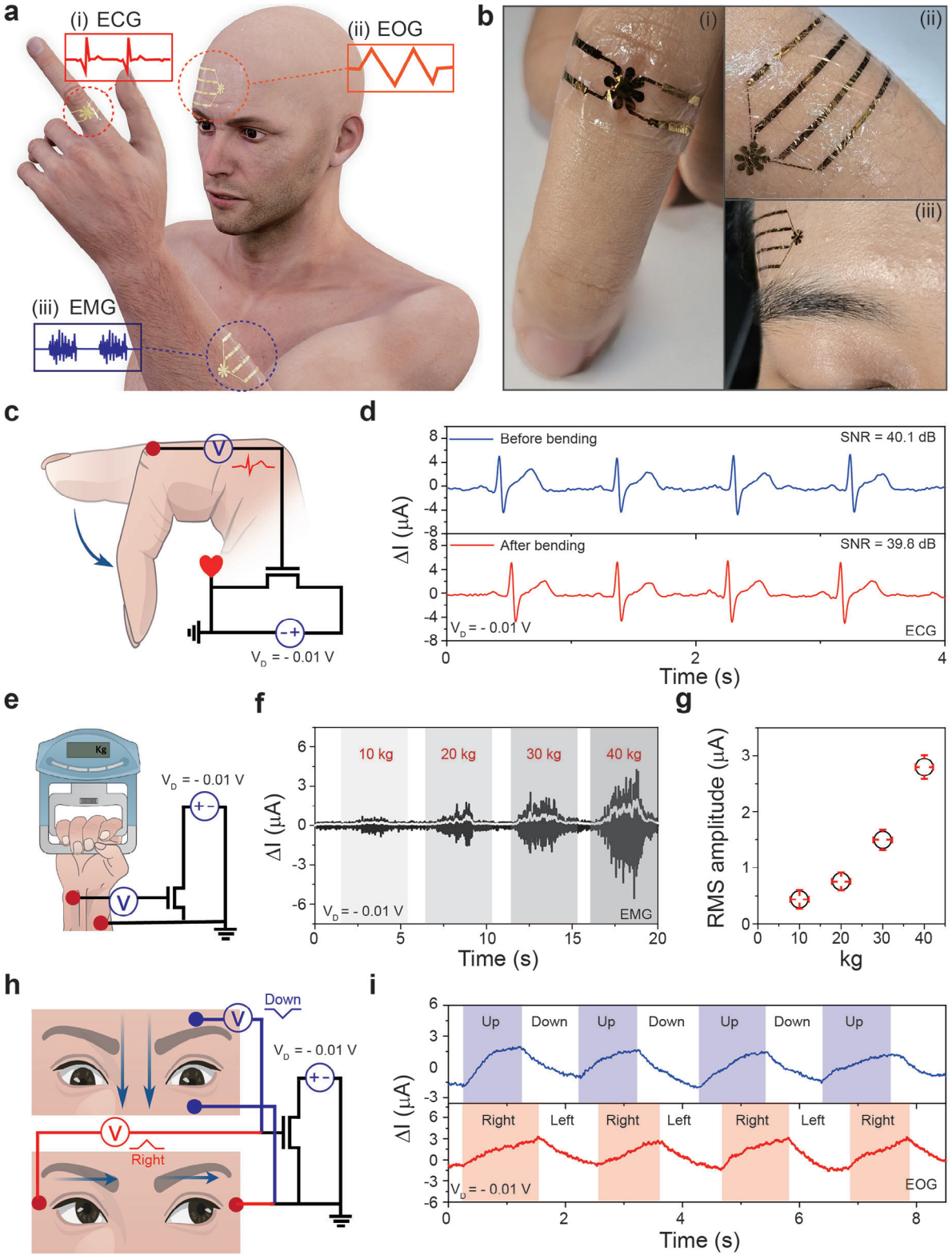

Figure 4. Physiological monitoring via skin-compatible 4-T vcOECT. a) Schematic of the skin-attached vcOECTs for physiological (ECG, EMG, EOG) signal monitoring. b) Photograph of the skin-conformable 4-T vcOECT on the complex skin surfaces. c) ECG monitoring circuit schematic. d) Monitoring of ECG signals before and after bending on index finger. e) EMG monitoring circuit schematic. f) Monitoring of the EMG signal on gripping a pressure device. EMG signals extracted by applying force to the pressure device of 10, 20, 30, and 40 kg. g) Variations of the EMG signal amplitude according to gripping force. h) EOG monitoring circuit schematic. i) Monitoring of EOG signals during up – down (blue) and right – left (red) eye movements.

We first demonstrate the application of OECTs in ECG signal monitoring. The ECG signal is a small electrical signal generated by the depolarization and repolarization of the cardiac muscle. Because the ultraflexible 4-T vcOECTs exhibited mechanical durability (Figure 3d,e), stable signal acquisition was verified when the sensor was directly attached to the top surface of the index finger. Moreover, measurements were secured even during joint movements, where the sensor was stretched (Figure 4c). As shown in Figure 4d, ECG signals, measured with very low $V_D = -0.01$ V and $V_G = 0$ V bias for 4 s, exhibited a high SNR of 40.1 and 39.5 dB for before and after joint movements (Note S4, Supporting Information), which was attributed to the low skin interface impedance due to the skin conformability of ultraflexible 4-T vcOECT. Moreover, long-term ECG measurements were conducted, showing that stable ECG signals were maintained for up to 30 min of continuous measurement without loss of SNR (Figure S24, Supporting Information). The seamless contact between device and skin extended the evaporation time of electrolyte, enabling reliable long-term signal acquisition without any hydrogel or ionic gel-based electrolyte. The device also exhibited stable shelf-life characteristics, remaining ready-to-use for over 60 h (Figure S25, Supporting Information). In contrast to conventional rigid sensors that are susceptible to the influence of motion artifacts owing to frictional electrification effects, the proposed ultraflexible 4-T vcOECTs established a stable electrical contact between the skin surfaces and demonstrated impervious effects on motion artifacts.

In our second application, we showcased EMG signal monitoring using the ultraflexible 4-T vcOECT as an EMG sensor. This device captures the electrical activity derived from neuromuscular activities culminating in muscle contractions. Drawing parallels to our earlier ECG detection experiments, force application on a muscle may alter EMG signal recordings due to the movement of the wrist muscle. The ultraflexible 4-T vcOECT enhances electrical contact with the skin, reducing motion artifacts from muscle tremors, and leading to a more precise EMG signal acquisition. As shown in Figure 4e, the muscles inside the wrist contracted to induce an EMG signal depending on the force applied to the gripping device. To confirm that the proposed flexible device could sensitively monitor EMG signals following muscle contraction at low driving voltages, forces of 10, 20, 30, and 40 kg were applied to the gripping device Figure 4f shows that the peak-to-peak amplitude and signal intensity of the EMG signal increased with the applied force at low driving voltages ($V_D = -0.01$ V) and $V_G = 0$ V bias for 20 s. Due to the fast response enabled by the compact active structure of vcOECTs, high-frequency spikes can be recorded without significant signal lag. The reduced channel dimensions also contribute to a more streamlined footprint for integrated single devices compared to conventional planar designs. The analysis of the root mean square (RMS) value of each applied force and the corresponding EMG signal indicated that, the higher the applied force, the higher the RMS value, and the lower the amplitude of the EMG signal generated by the smaller force that can be detected (Figure S26, Supporting Information).

Lastly, we showcased EOG signal monitoring. Skin-attached, low-operational voltage-driven 4-T vcOECTs offer high sensitivity in tracking eye movements, making it valuable across various domains such as medical diagnostics, sleep studies, virtual reality, and driving safety. We investigated the suitability of the ultraflexible 4-T vcOECT for this application by measuring both horizontal and vertical eyeball movements. As shown in Figure 4h, horizontal (right and left) and vertical (upper and lower positions) eye movements induced EOG signals. Figure 4i shows the recorded signals for horizontal and vertical eye movements. The monitoring of electrical signals following vertical (blue) and lateral (red) eye movements revealed similar amplitude changes. Differences in non-identical eye movement amplitudes are expected to result from unequal eye movement positions and forces. Consequently, the EOG signals that exhibited current changes in the range of a few microamperes at low driving voltages ($V_D = -0.01$ V) and $V_G = 0$ V bias for 9 s confirmed the feasibility of real-time monitoring of eye movements. Overall, the skin-compatible ultraflexible 4-T vcOECT underscores its unique advantages, which are attributed to its high sensitivity, mechanical durability, and low operational voltages, positioning it ideally for skin-interfaced electronic devices.

6. Conclusion

In conclusion, our research has successfully pushed the boundaries of skin-interfaced physiological sensors by introducing an innovative 4-T design incorporating vertical Corbino OECTs. This unique configuration empowers us to overcome persistent challenges associated with parasitic resistance, marking a significant advance in measuring the intrinsic properties of newly synthesized materials within a device platform. The durability and resilience of the device, even under significant strain, further accentuate its potential for real-world applications, especially in wearable health monitoring systems. Our device's ability to operate efficiently at ultralow voltages while maintaining high signal-to-noise ratios sets a new benchmark in non-invasive health monitoring. By seamlessly capturing essential physiological signals like ECG, EMG, and EOG, our advanced OECT promises transformative implications for the future of epidermal biosignal sensing. As the demand for non-intrusive health monitoring systems escalates, innovations such as ours pave the way for more sophisticated, durable, and efficient wearable devices.

7. Experimental Section

Ultraflexible pOECT and vcOECT Fabrication: To fabricate the ultraflexible substrates, the glass substrates were sequentially cleaned with detergent, deionized water, acetone, and isopropyl alcohol for 5 min each using ultrasonic treatment. To facilitate easy peeling from the glass substrate, a fluorinated polymer blended solution (Novec 1700:7100, 1:10 vol%, 3MTM) was spin-coated onto the glass substrate at 2000 rpm for 60 s, and a 1-µm-thick PaC film was deposited onto the surface of the fluorinated polymer/glass substrate through chemical vapor deposition. The 1-µm-thick PaC film was annealed at 120 °C for 1 h. For PaC film planarization, a 500-nm-thick epoxy (SU-8 3005, MicroChem) layer was spin coated at 5,000 rpm for 60 s and pre-baked at 95 °C for 2 min. Thereafter, the 500-nm-thick epoxy was exposed to UV light for 4 min and baked at 95 °C for 3 min. Finally, the 500-nm-thick epoxy was annealed at 120 °C for 1 h. Ultraflexible pOECT and vcOECT devices were fabricated as described above for the prepared SU-8/PaC substrate. The method of pOECT and vcOECT can be found in the Supporting Information. Devices were fabricated as described above for the prepared SU-8/PaC substrate.

Device Structure and Film Characterization: The vcOECT TEM image measured the cross-section of a vertical Corbino structure with a

channel radius of 70 µm and a channel length of 500 nm using a Tecnai G2 F30 S-Twin microscope operated at 300 kV. The SEM image of the ultraflexible vcOECT was obtained using a JSM-7900F microscope (Jeol, USA) operating at 15 kV. For the measurement, the ultraflexible vcOECT, laminated with a polymer elastomer (3 M VHB Y-4905J) pre-stretched to 200% and then compressed to a 50% strain, was loaded into the chamber. The Confocal images were obtained using an OLS3000 microscope with a 300 mm auto-stage. The analyses and plots were generated using Origin software.

Device Characterization and Analysis: Electrical characterization of the 2-terminal and 4-terminal OECTs was performed in two source-measure units (Keithley, 2400) under ambient conditions. All the electrical measurements were conducted in a phosphate-buffered saline (PBS) solution, the Ag/AgCl reference electrode immersed in KCl solution was used as the gate electrode. For both 2-terminal and 4-terminal measurements were conducted using identical device geometry regardless of pOECT or vcOECT, while measurement conditions were different. Detailed measurement setup is presented in Figure S1 (Supporting Information). To conduct 2-terminal measurement, the drain and source electrodes of the OECT devices were connected to the HI terminal and LO terminal of the source−measure units, respectively, for applying the drain voltage. The drain current of the device is measured by this source−measure unit. The Ag/AgCl gate electrode is connected to the HI terminal of another source-measure unit, which is used for applying the gate voltage to the OECT. The ground of the source−measure unit is shared by connecting both LO terminals to the source electrode of OECT. The measurement mode of source-measure unit for applying drain current is set to 2-wire sense mode. All the measurements were conducted by controlling the operation of source-measure unit using LabVIEW software. To conduct 4-terminal measurement, source, drain, and gate electrode connection is identical to the case of 2-terminal measurement, while the voltage probes ($V_{Sense,1}$ and $V_{Sense,2}$) are connected to the 4-wire sense connector of source-measure units for applying drain current, and the measurement mode of source−measure unit for applying drain current is set to 4-wire sense mode. All the source−measure unit and measurement parameters were controlled using LabVIEW software.

Frequency response of the 2-terminal and 4-terminal OECT devices was characterized by using a source-measure unit and oscilloscope/function generator equipment (Keysight Infinitives DSOX2002A). To perform the 2-terminal measurement, the drain and source electrodes of the OECT devices were connected to the HI terminal and LO terminals of the source−measure units, respectively, for applying the drain voltage. The Ag/AgCl gate electrode is connected to the oscilloscope/function generator equipment, which is used for applying the gate voltage to the OECT. To perform the 4-terminal measurement, source, drain, and gate electrode connection is identical to the case of 2-terminal measurement, while the voltage probes ($V_{Sense,1}$ and $V_{Sense,2}$)) are connected to the 4-wire sense connector of source−measure units, and the measurement mode of source−measure unit is set to 4-wire sense mode. A sinusoidal V_G signal (frequency range from 1 Hz to 10 kHz) with an amplitude of 50 mV was applied at offset potential where the maximum g_m was observed using a function generator. The drain current trace under a constant V_D was recorded using an SR570 preamplifier (Stanford Research Systems) and an oscilloscope. The transconductance was calculated as $\Delta I_D/\Delta V_G$, and the cutoff frequency was defined as the point where the transconductance value decreases by −3 dB from its initial value.

Mechanical Stability Test of Stretchable vcOECT: The freestanding ultraflexible vcOECT device was laminated with 200% outward pre stretched polymeric elastomer and placed in a compression machine. To accurately measure the electrical signal of the flexible device after peeling, the device pad was connected to an external wire using a Cr/Au (10/50 nm) line pattern. External wiring was deposited on a 3-µm-thick polyimide film through thermal evaporation. The contact between the device and the Au wiring was made with electrically conductive double-sided tape (3 M 9703-0.25″-36YDS). All mechanical stability tests were performed in PBS solution on polymer elastomers, and the Ag/AgCl reference electrode immersed in KCl solution was used as the gate electrode. Mechanical strains were measured using a compression machine, with the edges of the Au wires connected to alligator clips. A drain bias was applied via a source meter (Keithley 2400) connected to the Au wire.

ECG, EMG, and EOG Signal Measurement: To monitor ECG measurements, an ultraflexible device was attached to the right index finger using a drop of PBS solution, and source contact was established with the left chest using a gel electrode. For EMG measurements, the ultraflexible device was attached to the inner left wrist using a drop of PBS solution, and source contact was established with the inner right wrist using a gel electrode. To monitor EOG measurements, the ultraflexible device was attached to the upper and left areas around the eye using a drop of PBS solution, and source contact was established with the lower and right areas around the eye using a gel electrode. The connection to the gel electrode was made by linking the device pad to an external wire featuring a Cr/Au (10/50 nm) line pattern, fabricated using the same manufacturing method as the stretchable vcOECT measurements. The edge of the Au wire was connected to an alligator clip, which was attached to the gel electrode. The drain bias for the ECG, EMG, and EOG signals was applied using a source meter (Keithley 2400) connected to the Au wire. The ECG, EMG, and EOG signals were recorded at a sampling rate of 1 kHz using an SR570 preamplifier (Stanford Research Systems) and a data acquisition system (DAQ). The SR570 preamplifier was connected to the Au wire attached to the gel electrode. ECG signals were collected using a signal recording setup processed with a low-pass filter at 30 Hz. EMG signals were collected using a signal recording setup processed with a band-pass filter ranging from 1 to 300 Hz. EOG signals were collected using a signal recording setup processed with a low-pass filter at 30 Hz. The SNR was calculated as the ratio of the peak signal current to the standard deviation of the current between two peaks. All participants for the skin-conformal biosignal sensing experiments were co-authors of this manuscript and provided informed consent, who were approved by the Ajou University Institutional Review Board.

Supporting Information

Supporting Information is available from the Wiley Online Library or from the author.

Acknowledgements

This work was supported by the Ministry of Science and ICT grant funded by the Korean government (MSIT) (No. RS-2024-00411904). This research was supported by the Nano & Material Technology Development Program through the Ministry of Science and ICT grant funded by the Korean government (MSIT) (No. RS-2024-00403639). This work was supported by the Ajou University research fund.

Conflict of Interest

The authors declare no conflict of interest.

Author Contributions

I.L., J.H.K., and Y.K. contributed equally to this work. M.-H.Y. and S.P. conceived the idea for this work. I.L., Y.K., J.H.K., M.-H.Y., and S.P. designed the experiments and wrote the manuscript. I.L., D.S., H.L., J.-G.C., and J.W. fabricated the pOECT and vcOECT samples and conducted related electrical and mechanical experiments. I.L. fabricated the ultrathin vcOECT sample and conducted physiological signal acquisition. M.-H.Y., K.K., and S.P. oversaw the project, revised the manuscript, and led the effort to completion.

Data Availability Statement

The data that support the findings of this study are available from the corresponding author upon reasonable request.

Keywords

organic electrochemical transistor, organic mixed ionic–electronic conductor, ultraflexible device, vertical device

Received: July 18, 2024
Revised: October 11, 2024
Published online: November 3, 2024

[1] M. Ghittorelli, L. Lingstedt, P. Romele, N. I. Crăciun, Z. M. Kovács-Vajna, P. W. M. Blom, F. Torricelli, *Nat. Commun.* **2018**, *9*, 1441.
[2] P. Romele, P. Gkoupidenis, D. A. Koutsouras, K. Lieberth, Z. M. Kovács-Vajna, P. W. M. Blom, F. Torricelli, *Nat. Commun.* **2020**, *11*, 3743.
[3] Y. Deng, H. Qi, Y. Ma, S. Liu, M. Zhao, Z. Guo, Y. Jie, R. Zheng, J. Jing, K. Chen, H. Ding, G. Lv, K. Zhang, R. Li, H. Cheng, L. Zhao, X. Sheng, M. Zhang, L. Yin, *Proc. Natl. Acad. Sci. U.S.A.* **2022**, *119*, 2208060119.
[4] A. Takemoto, T. Araki, K. Nishimura, M. Akiyama, T. Uemura, K. Kiriyama, J. M. Koot, Y. Kasai, N. Kurihira, S. Osaki, S. Wakida, J. M. J. Den Toonder, T. Sekitani, *Adv. Sci.* **2023**, *10*, 2204746.
[5] M. Massetti, S. Zhang, P. C. Harikesh, B. Burtscher, C. Diacci, D. T. Simon, X. Liu, M. Fahlman, D. Tu, M. Berggren, S. Fabiano, *npj Flex Electron* **2023**, *7*, 11.
[6] B. Lin, M. Wang, C. Zhao, S. Wang, K. Chen, X. Li, Z. Long, C. Zhao, X. Song, S. Yan, L. Wang, W. Ma, *npj Flex Electron* **2022**, *6*, 77.
[7] Y. Yao, W. Huang, J. Chen, X. Liu, L. Bai, W. Chen, Y. Cheng, J. Ping, T. J. Marks, A. Facchetti, *Adv. Mater.* **2023**, *35*, 2209906.
[8] S. Park, S. W. Heo, W. Lee, D. Inoue, Z. Jiang, K. Yu, H. Jinno, D. Hashizume, M. Sekino, T. Yokota, K. Fukuda, K. Tajima, T. Someya, *Nature* **2018**, *561*, 516.
[9] M. Cucchi, C. Gruener, L. Petrauskas, P. Steiner, H. Tseng, A. Fischer, B. Penkovsky, C. Matthus, P. Birkholz, H. Kleemann, K. Leo, *Sci. Adv.* **2021**, *7*, eabh0693.
[10] S. Y. Yeung, X. Gu, C. M. Tsang, S. W. Tsao, I. Hsing, *Sens. Actuators, A* **2019**, *287*, 185.
[11] T. Li, J. Y. Cheryl Koh, A. Moudgil, H. Cao, X. Wu, S. Chen, K. Hou, A. Surendran, M. Stephen, C. Tang, C. Wang, Q. J. Wang, C. Y. Tay, W. L. Leong, *ACS Nano* **2022**, *16*, 12049.
[12] M. Braendlein, T. Lonjaret, P. Leleux, J.-M. Badier, G. G. Malliaras, *Adv. Sci.* **2017**, *4*, 1600247.
[13] R. B. Rashid, W. Du, S. Griggs, I. P. Maria, I. McCulloch, J. Rivnay, *Sci. Adv.* **2021**, *7*, eabh1055.
[14] W. Lee, S. Kobayashi, M. Nagase, Y. Jimbo, I. Saito, Y. Inoue, T. Yambe, M. Sekino, G. G. Malliaras, T. Yokota, M. Tanaka, T. Someya, *Sci. Adv.* **2018**, *4*, eaau2426.
[15] J. Brodský, I. Gablech, L. Migliaccio, M. Havlíček, M. J. Donahue, E. D. Głowacki, *ACS Appl. Mater. Interfaces* **2023**, *15*, 27002.
[16] W. Huang, J. Chen, Y. Yao, D. Zheng, X. Ji, L.-W. Feng, D. Moore, N. R. Glavin, M. Xie, Y. Chen, R. M. Pankow, A. Surendran, Z. Wang, Y. Xia, L. Bai, J. Rivnay, J. Ping, X. Guo, Y. Cheng, T. J. Marks, A. Facchetti, *Nature* **2023**, *613*, 496.
[17] Y. Yan, Q. Chen, X. Wu, X. Wang, E. Li, Y. Ke, Y. Liu, H. Chen, T. Guo, *ACS Appl. Mater. Interfaces* **2020**, *12*, 49915.
[18] W. Lee, D. Kim, J. Rivnay, N. Matsuhisa, T. Lonjaret, T. Yokota, H. Yawo, M. Sekino, G. G. Malliaras, T. Someya, *Adv. Mater.* **2016**, *28*, 9722.
[19] W. Lee, D. Kim, N. Matsuhisa, M. Nagase, M. Sekino, G. G. Malliaras, T. Yokota, T. Someya, *Proc. Natl. Acad. Sci. USA* **2017**, *114*, 10554.
[20] G. D. Spyropoulos, J. N. Gelinas, D. Khodagholy, *Sci. Adv.* **2019**, *5*, eaau7378.
[21] J. Wang, S. Lee, T. Yokota, T. Someya, *Adv. Funct. Mater.* **2022**, *32*, 2200458.
[22] S. Chen, K. Hou, T. Li, X. Wu, Z. Wang, L. Wei, W. L. Leong, *Adv. Mater. Technol.* **2023**, *8*, 2200611.
[23] J. T. Friedlein, R. R. McLeod, J. Rivnay, *Org. Electron.* **2018**, *63*, 398.
[24] J. Rivnay, P. Leleux, M. Ferro, M. Sessolo, A. Williamson, D. A. Koutsouras, D. Khodagholy, M. Ramuz, X. Strakosas, R. M. Owens, C. Benar, J.-M. Badier, C. Bernard, G. G. Malliaras, *Sci. Adv.* **2015**, *1*, e1400251.
[25] M. Gryszel, D. Byun, B. Burtscher, T. Abrahamsson, J. Brodsky, D. T. Simon, M. Berggren, E. D. Glowacki, X. Strakosas, M. J. Donahue, *J. Mater. Chem. C* **2024**, *12*, 5339.
[26] Y. Dai, S. Dai, N. Li, Y. Li, M. Moser, J. Strzalka, A. Prominski, Y. Liu, Q. Zhang, S. Li, H. Hu, W. Liu, S. Chatterji, P. Cheng, B. Tian, I. McCulloch, J. Xu, S. Wang, *Adv. Mater.* **2022**, *34*, 2201178.
[27] Y. Kim, G. Kim, B. Ding, D. Jeong, I. Lee, S. Park, B. J. Kim, I. McCulloch, M. Heeney, M. Yoon, *Adv. Mater.* **2022**, *34*, 2107355.
[28] L. Wang, Q. Sun, L. Zhang, J. Wang, G. Ren, L. Yu, K. Wang, Y. Zhu, G. Lu, H. Yu, *Macromol. Rapid Commun.* **2022**, *43*, 2200212.
[29] X. Wu, M. Stephen, T. C. Hidalgo, T. Salim, J. Surgailis, A. Surendran, X. Su, T. Li, S. Inal, W. L. Leong, *Adv. Funct. Mater.* **2022**, *32*, 2108510.
[30] S.-M. Kim, C.-H. Kim, Y. Kim, N. Kim, W.-J. Lee, E.-H. Lee, D. Kim, S. Park, K. Lee, J. Rivnay, M.-H. Yoon, *Nat. Commun.* **2018**, *9*, 3858.
[31] M. J. Donahue, A. Williamson, X. Strakosas, J. T. Friedlein, R. R. McLeod, H. Gleskova, G. G. Malliaras, *Adv. Mater.* **2018**, *30*, 1705031.
[32] H. Lee, S. Lee, W. Lee, T. Yokota, K. Fukuda, T. Someya, *Adv. Funct. Mater.* **2019**, *29*, 1906982.
[33] P. Leleux, J. Rivnay, T. Lonjaret, J.-M. Badier, C. Bénar, T. Hervé, P. Chauvel, G. G. Malliaras, *Adv. Healthcare Mater.* **2015**, *4*, 142.
[34] J. Fan, C. Montemagno, M. Gupta, *Org. Electron.* **2019**, *73*, 122.
[35] J. Kim, R. M. Pankow, Y. Cho, I. D. Duplessis, F. Qin, D. Meli, R. Daso, D. Zheng, W. Huang, J. Rivnay, T. J. Marks, A. Facchetti, *Nat. Electron.* **2024**, *7*, 234.
[36] A. G. Polyravas, V. F. Curto, N. Schaefer, A. B. Calia, A. Guimera-Brunet, J. A. Garrido, G. G. Malliaras, *Flex. Print. Electron.* **2019**, *4*, 044003.
[37] J. H. Kim, Z. Ahmad, Y. Kim, W. Kim, H. Ahn, J.-S. Lee, M.-H. Yoon, *Chem. Mater.* **2020**, *32*, 8606.
[38] J. H. Kim, M. Wieland, B. Omiecienski, Y. Kim, J. Park, G. Kim, S. Ludwigs, M.-H. Yoon, *Flex. Print. Electron.* **2022**, *7*, 044005.
[39] J. Rivnay, S. Inal, B. A. Collins, M. Sessolo, E. Stavrinidou, X. Strakosas, C. Tassone, D. M. Delongchamp, G. G. Malliaras, *Nat. Commun.* **2016**, *7*, 11287.
[40] B. Wang, Y. Kong, S. Zhang, Z. Wu, S. Wang, J. Ren, H. Y. Woo, Y. Li, W. Ma, *Adv. Funct. Mater.* **2024**, *34*, 2312822.
[41] J. H. Kim, R. Halaksa, I.-Y. Jo, H. Ahn, P. A. Gilhooly-Finn, I. Lee, S. Park, C. B. Nielsen, M.-H. Yoon, *Nat. Commun.* **2023**, *14*, 7577.
[42] A. Savva, C. Cendra, A. Giugni, B. Torre, J. Surgailis, D. Ohayon, A. Giovannitti, I. McCulloch, E. Di Fabrizio, A. Salleo, J. Rivnay, S. Inal, *Chem. Mater.* **2019**, *31*, 927.
[43] S. Zhang, P. Ding, T. Ruoko, R. Wu, M. Stoeckel, M. Massetti, T. Liu, M. Vagin, D. Meli, R. Kroon, J. Rivnay, S. Fabiano, *Adv. Funct. Mater.* **2023**, *33*, 2302249.
[44] Y. Liu, H. Zhou, R. Cheng, W. Yu, Y. Huang, X. Duan, *Nano Lett.* **2014**, *14*, 1413.
[45] A. Chortos, Z. Bao, *Mater. Today* **2014**, *17*, 321.
[46] R. Maiti, L.-C. Gerhardt, Z. S. Lee, R. A. Byers, D. Woods, J. A. Sanz-Herrera, S. E. Franklin, R. Lewis, S. J. Matcher, M. J. Carré, *J. Mech. Behav. Biomed. Mater.* **2016**, *62*, 556.
[47] J. Jeong, W. Yeo, A. Akhtar, J. J. S. Norton, Y. Kwack, S. Li, S. Jung, Y. Su, W. Lee, J. Xia, H. Cheng, Y. Huang, W. Choi, T. Bretl, J. A. Rogers, *Adv. Mater.* **2013**, *25*, 6839.